PAPER

Check for updates

A new melilite-type rare-earth borate $CdTbGaB_2O_7$ and multicolor tunable emission in the $CdTb_{1−x}Sm_xGaB_2O_7$ ($0 \leq x \leq 0.2$) phosphors†

Xuean Chen, [ID] *[a] Jinyuan Zhang,[a] Weiqiang Xiao[b] and Xiaoyan Song [ID] [a]

A new mixed metal borate, $CdTbGaB_2O_7$, was successfully synthesized using the high-temperature solution method and its crystal structure was determined by single-crystal X-ray diffraction with the following unit-cell data: $P\bar{4}2_1m$, $a = b = 7.3487(1)$ Å, $c = 4.7247(1)$ Å, $V = 255.150(9)$ Å^3, and $Z = 2$. It belongs to a new member of the melilite family, which features a 3D framework consisting of alternately stacked $[Ga(B_2O_7)]_n^{5n−}$ tetrahedral layers and (Cd^{2+}/Tb^{3+}) cationic layers that are interconnected via B(Ga)−O−(Cd/Tb) bridges. In addition, the solid solutions of $CdTb_{1−x}Sm_xGaB_2O_7$ ($0 \leq x \leq 0.2$) were prepared via the solid-state reaction method. The combined techniques of XRD, SEM, IR/Raman, XPS and PLE/PL were employed to characterize the products. It was found that the $CdTb_{1−x}Sm_xGaB_2O_7$ phosphors simultaneously showed green emission of Tb^{3+} at 545 nm and orange emission of Sm^{3+} at 603 nm under excitation at 370 nm. The emission color can be adjusted from green to orange-red by varying the Sm^{3+} doped content via an energy transfer mechanism. For $CdTb_{0.995}Sm_{0.005}GaB_2O_7$, a QY of 13.22% was obtained, and its emission intensity at 423 K was 94% of that at 303 K. These results show that the prepared materials can act as potential color-tunable phosphors for UV w-LEDs.

1. Introduction

Melilites include a large class of natural and synthetic compounds, whose general formula is $A_2XZ_2O_7$, where A cations (A = Na, Ca, Sr, Ba, Cd, Pb, Y, Ln) are sandwiched between XZ_2O_7 tetrahedral layers (X = Be, Mg, Co, Fe, Mn, Cu, Zn, Cd, Al, Ga; Z = Be, B, Al, Ga, Si, Ge).[1] The melilite-like compounds have been extensively investigated in the past due to their crystal chemical properties and potential applications. For example, crystallographic studies indicated that the stability of the melilite structure depends strongly on the degree of the size misfit between the tetrahedral layers and the interlayer cations.[2]

[a]Faculty of Materials and Manufacturing, Key Laboratory of Advanced Functional Materials, Ministry of Education of China, Beijing University of Technology, 100124 Beijing, China. E-mail: xueanchen@bjut.edu.cn

[b]Beijing Key Laboratory of Microstructure and Property of Solids, Beijing University of Technology, 100124 Beijing, China

† Electronic supplementary information (ESI) available: The X-ray crystallographic file for $CdTbGaB_2O_7$ in CIF format; atomic coordinates, equivalent isotropic and anisotropic displacement parameters; selected bond distances and angles; correlation table of B_2O_7 between the site group of the molecule (C_{2v}) and the factor group of the crystal (D_{2d}); Rietveld refinement results of $CdTb_{1−x}Sm_xGaB_2O_7$ ($0 \leq x \leq 1$); the SEM image and EDX results of the $CdTbGaB_2O_7$ single-crystal; Rietveld refinements of powder X-ray diffractograms of $CdTb_{1−x}Sm_xGaB_2O_7$ ($0.001 \leq x \leq 0.2$); IR, Raman, XPS and UV-vis absorption spectra; the excitation line of $BaSO_4$ and the PL spectrum of the $CdTb_{0.995}Sm_{0.005}GaB_2O_7$ phosphor. CCDC 2253832. For ESI and crystallographic data in CIF or other electronic format see DOI: https://doi.org/10.1039/d3ra03002d

As far as their application prospects are concerned, some Si (or Ge)-based melilites may act as potential microwave dielectric materials.[3] Doped with Nd^{3+}, crystals of the melilite family, *e.g.* $Ca_2Ga_2SiO_7$, $Ba_2MgGe_2O_7$ and $Ba_2ZnGe_2O_7$, were successfully used in high-power lasers, both with Xe-flash lamp pumping and with laser-diode pumping.[4-6]

The mineral okayamalite, $Ca_2SiB_2O_7$, was first discovered by Giuli *et al.* in 2000, which is the only melilite borate known at early times.[7] Subsequently, Barbier *et al.* conducted a systematic survey of several MO–Bi_2O_3 (and Ga_2O_3)–B_2O_3 systems and found three new diborate members of this family, including $Bi_2ZnB_2O_7$, $CaBiGaB_2O_7$, and $CdBiGaB_2O_7$ (only unit-cell data were provided for the last borate).[8] Among them, two Ga-containing compounds crystallize with the normal tetragonal melilite structure, whereas the Zn-containing phase adopts a unique orthorhombic superstructure of melilite. The attempted solid-state syntheses of the other melilites, such as $Bi_2MB_2O_7$ (M = Be, Mg, Co), $MBiGaB_2O_7$ (M = Mg, Sr, Ba), $CaBiMB_2O_7$ (M = B, Al, In), and $MBiZnB_2O_7$ (M = Y, Nd, Yb), were unsuccessful. The preliminary measurements of second-harmonic generation (SHG) efficiencies (d_{eff}) on powder samples yielded values of 4.0 ($Bi_2ZnB_2O_7$) and 1.6 ($CaBiGaB_2O_7$) relative to a KH_2PO_4 (KDP) standard. The larger efficiency of $Bi_2ZnB_2O_7$ was ascribed to the presence of planar BO_3 groups and a higher concentration of the heavy and polarizable Bi^{3+} cations in its crystal structure. Soon after, relatively large single crystals of $Bi_2ZnB_2O_7$ were successfully grown from a high-temperature melt by the top-seeded method, which reveals

that this borate is a promising candidate for nonlinear optical (NLO) materials.[9] This Zn-containing melilite diborate is still of current interest due to its potential value as a host to prepare different kinds of luminescent materials. For instance, Tb^{3+}, Sm^{3+}, Eu^{3+} and Dy^{3+}-doped $Bi_2ZnB_2O_7$ phosphors were synthesized and their luminescent properties were investigated.[10–12] When active laser medium (such as Er^{3+}, Nd^{3+} or Pr^{3+} ions) are doped into this crystal structure, the obtained crystals may show both luminescence and NLO properties, which makes them very attractive for the new generation of laser frequency converters, the representative crystals including $Bi_2ZnOB_2O_6$:Yb^{3+}/Er^{3+}, $Bi_2ZnOB_2O_6$:Nd^{3+} and $Bi_2ZnOB_2O_6$:Pr^{3+}.[13–15] In addition, not long ago, two new melilite-type borogermanates, $Ca_2GeB_2O_7$ and $Ca_{1.78}Cd_{0.22}GeB_2O_7$, were also reported, among which $Ca_2GeB_2O_7$ has a short UV cutoff edge (<200 nm), indicating its potential as an optical material in the UV or DUV region.[16] The compounds mentioned above are the only borates with melilite structure reported so far. In contrast to many investigations on $Bi_2ZnB_2O_7$, there are no studies of $CaBiGaB_2O_7$ and $CdBiGaB_2O_7$ as promising hosts for luminescence applications, and also, there are no reports on rare-earth analogues of these borates in the literature.

It is well known that Tb^{3+} ions usually generate green emission arising from the $^5D_4 \rightarrow {}^7F_J$ ($J = 6, 5, 4, 3$) transitions, while Sm^{3+} ions emit orange-red light due to the $^4G_{5/2} \rightarrow {}^6H_J$ ($J = 5/2, 7/2, 9/2, 11/2$) transitions.[17] In Tb^{3+}/Sm^{3+} co-doped systems, terbium plays the role of a sensitizer, and samarium is an activator. The energy transfer from Tb^{3+} to Sm^{3+} occurs, which makes it possible to achieve the multicolor tunable luminescence from green to orange-red by simply adjusting the ratio of these two ions. With these materials, it will be more convenient to control the color output according to the practical application requirements. Therefore, the study of Tb^{3+}/Sm^{3+} co-doped phosphors is not only of theoretical but also of practical significance, and some previously reported examples are $KBaY(MoO_4)_3$:Ln^{3+} (Ln^{3+} = Tb^{3+}, Eu^{3+}, Sm^{3+}, Tb^{3+}/Eu^{3+}, Tb^{3+}/Sm^{3+}), $CaLa_2(MoO_4)_4$:Tb^{3+}/Sm^{3+}, and $Ba_3La(PO_4)_3$:Tb^{3+}/Sm^{3+}.[18–20]

In the process of exploring new borate materials to study their structure–property relationships, we found that Bi^{3+} in $CdBiGaB_2O_7$ can be completely replaced by Tb^{3+}, resulting in a new melilite diborate, $CdTbGaB_2O_7$. Insofar as we know, it represents the first quaternary compound within $CdO–Ln_2O_3–Ga_2O_3–B_2O_3$ (Ln = trivalent rare-earth cations) system, and it is also the only rare-earth borate of the melilite family known to date. In this work, we first performed the synthesis and characterization of $CdTbGaB_2O_7$, then introduced Sm^{3+} into $CdTbGaB_2O_7$ to prepare $CdTb_{1-x}Sm_xGaB_2O_7$ solid solutions (x = 0–0.2), and further studied the luminescence properties and energy transfer of Sm^{3+} doped $CdTbGaB_2O_7$. The obtained results suggest that this type of novel phosphors could serve as a multi-color component in UV w-LEDs.

2. Experimental section

2.1. Materials and methods

All chemicals, including $CdCO_3$ (A.R.), Tb_4O_7 (99.99%), $Tb(NO_3)_3 \cdot 6H_2O$ (A.R.), Sm_2O_3 (99.99%), Ga_2O_3 (99.99%) and

H_3BO_3 (A.R.), were commercially available from Sinopharm Chemical Reagent Co. Ltd and used without further purification. The XRD plots were recorded on a Bruker AXS D8 ADVANCE diffractometer equipped with Cu K$_{\alpha 1}$ radiation (λ = 1.5406 Å) operating at 40 kV and 40 mA. Surface morphology and element compositions of the synthetic product were characterized by a Hitachi SU8020 field emission scanning electron microscope (FE-SEM) equipped with an energy dispersive X-ray spectrometer (EDX). The Infrared (IR) spectra were measured with a Bruker VERTEX70 FT-IR spectrometer using the KBr pellet method. The Raman studies were carried out using a Renishaw InVia Raman spectrometer equipped with a confocal DM 2500 Leica optical microscope, a thermoelectrically cooled CCD as a detector, and He/Ne laser as an exciting source working at 633 nm. The X-ray photoelectron spectroscopy (XPS) measurements were done by a Thermo ESCALAB 250xi spectrometer equipped with Al Kα ($h\nu$ = 1486.6 eV) as an excitation source. The UV-vis absorption spectra were monitored using a Hitachi UH4150 spectrophotometer equipped with an integrating sphere attachment. The excitation and emission spectra as well as decay kinetics were investigated using an Edinburgh FLS 1000 system equipped with a 450 W Xe lamp and a 60 W μF flash lamp. Quantum yield (QY) and temperature-dependent emission spectra were determined by the same spectrometer with a $BaSO_4$-coated integrating sphere and a temperature controlling system, respectively.

2.2. Synthetic procedures

Single crystals of $CdTbGaB_2O_7$ were grown by the high-temperature solution method. In a typical procedure, a powder mixture of 0.5464 g $CdCO_3$, 0.1974g Tb_4O_7, 0.4950 g Ga_2O_3 and 0.2612 g H_3BO_3 (molar ratio 12 : 1 : 10 : 16) was thoroughly ground and placed in a Pt crucible. The mixture was slowly heated to 950 °C in a muffle furnace, and maintained at this temperature for 6 h to ensure that the raw materials are completely melted and uniformly mixed. Subsequently, the solution temperature was decreased, first to 700 °C at a rate of 1.5 °C h^{-1}, then to 400 °C at 5.0 °C h^{-1}, and finally to room temperature at 20 °C h^{-1}. Many colorless, transparent, block-shaped crystals were obtained. Energy-dispersive X-ray analysis in a scanning electron microscope confirmed that the crystal contains the elements Cd, Tb, Ga, and O with an approximate atomic ratio of 10.44 : 8.25 : 6.65 : 74.66, which is close to its ideal composition of 1 : 1 : 1 : 7 (B is too light to be detected, see Fig. S1†).

The powder samples of $CdTb_{1-x}Sm_xGaB_2O_7$ (x = 0, 0.001, 0.002, 0.005, 0.01, 0.05, 0.1, 0.2, and 1) were obtained through solid-state reactions of the calculated amounts of $CdCO_3$, $Tb(NO_3)_3 \cdot 6H_2O$, Sm_2O_3, Ga_2O_3, and H_3BO_3. The well-ground samples were first preheated at 500 °C for 12 h and then sintered at 800 °C for 120 h with several intermediate re-mixings. Finally, the as-synthesized samples were ground into fine powder and their phase purity was checked by powder X-ray diffraction.

2.3. Single-crystal X-ray diffraction

Single-crystal diffraction data were collected at room temperature on an Agilent Super Nova diffractometer equipped with

Table 1 Crystallographic data for $CdTbGaB_2O_7^a$

Formula	$CdTbGaB_2O_7$
Formula weight	474.66
Space group	$P\bar{4}2_1m$ (No. 113)
a (Å)	7.3487(1)
c (Å)	4.7247(1)
V (Å³)	255.150(9)
Z	2
d_{calc} (g cm⁻³)	6.178
μ (mm⁻¹)	23.062
$2\theta_{max}$ (°)	69.94
Unique reflections	620
Observed $[I \geq 2\sigma(I)]$	598
No. of variables	35
GOF on F_o^2	1.092
R_1/wR_2 $[I \geq 2\sigma(I)]$	0.0221/0.0443
R_1/wR_2 (all data)	0.0236/0.0449
$\Delta\rho_{max}$, $\Delta\rho_{min}$ (e Å⁻³)	1.528, −1.379

^{a} $R_1 = \Sigma||F_o| - |F_c||/\Sigma|F_o|$ and $wR_2 = [\Sigma w(F_o^2 - F_c^2)^2/\Sigma wF_o^4]^{1/2}$ for $F_o^2 > 2\sigma(F_o^2)$.

a Mo X-ray source (λ = 0.71073 Å). The data collection and reduction were performed with the CrysAlisPro software, and absorption corrections were made by the multi-scan method.[21] The crystal structure was established by Direct Methods and subsequently refined by the full-matrix least-squares method on F^2 on the basis of SHELX-2018.[22] All atoms were refined anisotropically and the final difference Fourier synthesis did not reveal any significant residual peaks.

Refinements of atomic occupancy parameters indicated that Cd and Tb atoms reside in the same atomic site (Wyckoff 4e) with the composition $Cd_{0.5}Tb_{0.5}$, which is not surprising since Cd^{2+} and Tb^{3+} have similar cationic radii (1.10 Å for Cd^{2+} vs. 1.04 Å for Tb^{3+}, CN = 8) and coordination geometries.[23] For this (Cd/Tb) site, no abnormally large displacement parameters were observed, and the largest principal anisotropic displacement parameter $[U_{11} = U_{22} = 0.01079(11)$ Å²$]$ was only about 1.3 times of the smallest one $[U_{33} = 0.00832(13)$ Å²$]$ (Table S2†). Therefore, it is not necessary to split (Cd/Tb) into two positions. In addition, the single-crystal XRD data did not show a symmetry lower than tetragonal or a larger unit cell that would allow the ordering of Cd^{2+}/Tb^{3+}. Finally, the disorder model was adopted. The flack parameter of this compound was refined to be −0.12(4). The program PLATON was used to check the positional parameters,[24] and no higher symmetries were found. Details of unit-cell parameters, data collection and structure refinements are summarized in Table 1. Atomic coordinates and equivalent isotropic and anisotropic displacement parameters are given in Tables S1 and S2† and selected bond lengths and angles in Table S3.†

3. Results and discussion

3.1. Crystal structure description

$CdTbGaB_2O_7$ is a new member of the melilite series, and it is also the only rare-earth borate of this family known so far. In this structure, two BO_4 tetrahedra first share a corner to form a diborate group, $[B_2O_7]^{8-}$. Each $[B_2O_7]^{8-}$ dimer is linked to four different GaO_4 tetrahedra, and, likewise, each GaO_4 tetrahedron is connected to four neighboring $[B_2O_7]^{8-}$ groups via common O atoms to form a 2D infinite $[Ga(B_2O_7)]_n^{5n-}$ layer extending in the (001) plane [see Fig. 1(b)]. These gallium borate anionic layers are stacked along the crystallographic c-axis direction, and (Cd^{2+}/Tb^{3+}) cations are placed in the square antiprismatic cavities between the layers to hold them together via (Cd/Tb)–O bonds, thus obtaining a 3D $[CdTbGa(B_2O_7)]_n$ framework [Fig. 1(a)].

As shown in Table S1,† the asymmetric unit of $CdTbGaB_2O_7$ contains one disordered (Cd/Tb), one Ga, one B and three O sites. Among them, each (Cd/Tb) has eight O nearest-neighbors arranged into a distorted square antiprism [Fig. 1(c)]. The (Cd/Tb)–O distances fall in the range of 2.305(4)–2.547(3) Å, with an average of 2.430 Å (Table S3†), which lies between 2.42 and 2.48 Å computed from crystal radii sums of Tb^{3+} and O^{2-} as well as Cd^{2+} and O^{2-} for 8-fold coordination, respectively.[23] These distances also correspond to those found in α-$CdUO_4$, $CdPd_3O_4$ and $Ba_2CdTb_2(BO_3)_4$, where 8-coordinated Cd^{2+} or Tb^{3+} exist.[25–27] Both Ga and B atoms adopt a tetrahedral coordination configuration. However, the Ga atom is located on the $\bar{4}$ axis, thereby resulting in four equal Ga–O bond lengths of 1.824(3) Å and two groups of O–Ga–O bond angles of 107.90(10)° and 112.7(2)°, while the B atom lies on a mirror plane, giving three groups of B–O distances of 1.419(7), 1.492(7) and 1.525(5) Å and four groups of O–B–O angles of 114.6(5)°, 116.1(3)°, 102.6(3)° and 102.9(4)°. The average O–Ga–O and O–B–O angles are 109.5° and 109.15°, respectively, indicating that the GaO_4 tetrahedron is rather regular, while the BO_4 is somewhat deformed (Table S3†). Similar GaO_4 and BO_4 groups have already been identified in $K_2Ga_2O(BO_3)_2$ and $In_4O_2B_2O_7$, respectively.[28,29] Furthermore, the calculated bond valence sums are 3.10 for Ga^{3+} and 2.92 for B^{3+}, respectively, close to their expected values, indicating the validity of the structure.[30]

In the literature, several compounds with the chemical formula containing "B_2O_7" are known, which have various structure types from extended 2D layers to 3D frameworks. For example, all $Bi_2CaB_2O_7$, $Bi_2SrB_2O_7$ and $Bi_{1.48}Eu_{0.52}Pb_{0.5}Sr_{0.5}B_2$-$O_7$ contain topologically identical 2D $[A_2MO(BO_3)_2]$ [A = Bi, (Bi/Eu); M = Ca, Sr, (Pb/Sr)] layers built of corner-sharing $[BO_3]^{3-}$ triangles and $[MO_6]^{10-}$ trigonal prisms with $[A_2O]^{4+}$ groups accommodated within six-membered rings. However, the Ca and Sr compounds take an acentric structure with space groups $Pna2_1$ and $P6_3$, respectively, while the (Pb/Sr) phase crystallizes in the centrosymmetric $R\bar{3}c$ group.[31,32] $BaAl_2B_2O_7$ also has a layered structure, but being built up from $[BO_3]^{3-}$ triangles and $[Al_2O_7]^{8-}$ groups, and the latter consists of two corner-sharing AlO_4 tetrahedra.[33] $Bi_2ZnB_2O_7$ contains both tetrahedral $[B_2O_7]^{8-}$ and triangular $[B_2O_5]^{4-}$ diborate groups, which are alternately arranged in the a and b directions, and further bridged by tetrahedral Zn^{2+} centers through sharing three O atoms of each ZnO_4 tetrahedron to generate a 2D $[Zn_2O_2(B_2$-$O_7)(B_2O_5)]_n^{12n-}$ layer. These zinc borate anionic layers are held together by the octahedrally coordinated Bi^{3+} cations to create a 3D framework.[8] This is different from the case of $CdTbGaB_2$-O_7, where the 3D network is only composed of $[B_2O_7]^{8-}$
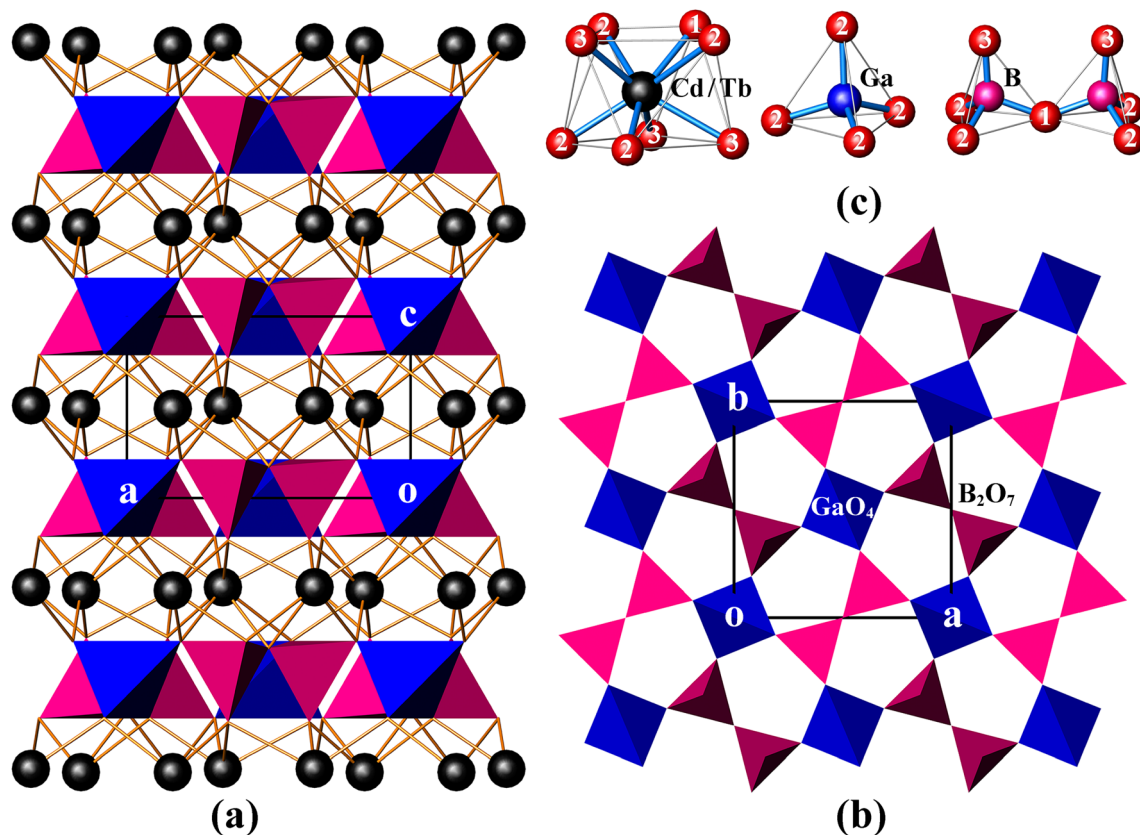
Fig. 1 The unit cell of CdTbGaB$_2$O$_7$ projected along [010] (a), the [Ga(B$_2$O$_7$)]$_n^{5n-}$ layer viewed along [001] (b), and the coordination environment of each cation site (the numbers correspond to the oxygen atom designations) (c). (Cd/Tb): black spheres; GaO$_4$: blue tetrahedra; BO$_4$: magenta tetrahedra.

tetrahedral dimers, GaO$_4$ tetrahedra, and 8-coordinated (Cd^{2+}/Tb^{3+}) cations, and each GaO$_4$ corner-shares with four [B$_2$O$_7$]$^{8-}$ units. It is the differences in the fundamental building blocks and their connection modes that make these structures significantly different, which enriches the structural chemistry of borates.

3.2. IR and Raman spectra

CdLnGaB$_2$O$_7$ (Ln = Tb, Sm) crystallizes in the tetragonal space group $P\bar{4}2_1m$ (D$_{2d}^3$, No. 113), and its primitive cell comprises two B$_2$O$_7$ "pyro" units. A free B$_2$O$_7$ group is composed of two corner-shared BO$_4$ tetrahedra, which can be described as two BO$_3$ groups connected by a bent B^{O}B bridge, as shown in Fig. 1(c). In analogy with pyrophosphate and pyrogermanate groups (P$_2$O$_7$ and Ge$_2$O$_7$),[34–36] the 21 internal modes of the free B$_2$O$_7$ group with C_{2v} symmetry can be subdivided into: A$_1$ + B$_1$ symmetric and A$_1$ + A$_2$ + B$_1$ + B$_2$ antisymmetric stretching modes of the BO$_3$ groups [ν_s(BO$_3$) and ν_{as}(BO$_3$), respectively]; A$_1$ symmetric and B$_1$ antisymmetric stretching modes of the B^{O}B bridge [ν_s(B^{O}B) and ν_{as}(B^{O}B), respectively]: A$_1$ bending mode of the B^{O}B bridge [δ(B^{O}B)]; A$_2$ + B$_2$ rocking modes of the BO$_3$ groups [ρ(BO$_3$)]; and 3A$_1$ + 2A$_2$ + 3B$_1$ + 2B$_2$ O–B–O bending modes [δ(BO$_3$)] (see the correlation diagram presented in Table S4†). In the crystal, these modes will give rise to 7A$_1$ + 4A$_2$ + 4B$_1$ + 7B$_2$ + 10E internal modes. Translational (T′) and librational (L)

modes of free B$_2$O$_7$, *i.e.* A$_1$ + B$_1$ + B$_2$ and A$_2$ + B$_1$ + B$_2$, transform in crystal into A$_1$ + B$_2$ + 2E and A$_2$ + B$_1$ + 2E external modes, respectively. In addition, the disordered (Cd/Tb) atoms occupy the 4e Wyckoff positions of C_s symmetry and Ga atoms the 2a positions of S$_4$ symmetry (Table S1†). These atoms contribute totally with 2A$_1$ + A$_2$ + 2B$_1$ + 3B$_2$ + 5E translational modes. By adding all these modes and subtracting three acoustic modes (B$_2$ + E), the following optical vibrational modes of the crystal can be obtained: Γ_{optic} = 10A$_1$ + 6A$_2$ + 7B$_1$ + 10B$_2$ + 18E, in which E modes are twofold degenerated and often observed as one frequency. Among these modes, B$_2$ and E are both IR- and Raman-active, A$_1$ and B$_1$ are Raman-active only, and A$_2$ is silent. This analysis shows that 63 modes in the Raman spectrum (10A$_1$ + 7B$_1$ + 10B$_2$ + 18E) and 46 modes in the IR spectrum (10B$_2$ + 18E) are expected to be observed, resulting in 45 Raman and 28 IR frequencies, respectively. Due to the large number of modes and the overlap of some modes, a precise assignment of the individual bands to specific vibrational modes is difficult, but a rough assignment of groups is possible for both IR and Raman spectra.

Fig. S2† shows the room-temperature IR and Raman spectra of the CdLnGaB$_2$O$_7$ (Ln = Tb, Sm) samples. Due to experimental limitations, IR characterization below 500 cm^{-1} is not possible. Two compounds exhibit similar spectral profiles, reflecting their isostructural features. The tentative band assignments are

based on literature data,[29,37–39] and the frequencies of the B_2O_7 group are assigned according to the characteristic vibrations of the B^OB bridge and the terminal BO_3 groups. The bands due to the antisymmetric BO_3 terminal stretching vibrations of the B_2O_7 group $[\nu_{as}(BO_3)]$ and the antisymmetric B^OB bridge stretching modes $[\nu_{as}(B^OB)]$ are observed in the high-frequency region of 1250–900 cm^{-1}. The intensities of these bands are generally greater in infrared than in Raman spectra.[38] The strong Raman bands at about 787 (795) cm^{-1} are assigned to the symmetric stretching of the terminal BO_3 groups $[\nu_s(BO_3)]$, while in infrared spectra, these vibrations are clearly observed in the region of 800–840 cm^{-1}. The IR bands near 704 (719) cm^{-1} can be attributed to the stretching vibrations of GaO_4 tetrahedra,[40,41] which matches with the peaks at 668 (676) cm^{-1} in the Raman spectra. The absorption bands at 600–300 cm^{-1} correspond to the $\delta(B^OB)$ and $\delta(BO_3)$ bending modes, and the bending vibrations of the GaO_4 tetrahedra also appear in this area, making it difficult to assign the bands below 600 cm^{-1}.[39,42] Thus, the IR and Raman spectra confirm the presence of B_2O_7 tetrahedral dimers and four-coordinated Ga^{3+} ions, in accordance with the results obtained from the single-crystal XRD analyses.

3.3. UV-vis absorption spectra

Fig. S3† shows the UV-visible absorption spectra of $CdLnGaB_2O_7$ (Ln = Tb, Sm) (converted from diffuse reflectance data). The spectrum of the Tb compound shows a wide absorption band superimposed with several weak absorption peaks below 500 nm, which are mainly attributed to the inter-configurational 4f–5d transitions and intra-configurational 4f–4f transitions of the Tb^{3+} ions, i. e. $^7F_6 \rightarrow {}^5L_8$ at 352 nm, $^7F_6 \rightarrow {}^5L_{10}$ at 370 nm, $^7F_6 \rightarrow {}^5D_3$ at 377 nm and $^7F_6 \rightarrow {}^5D_4$ at 489 nm, respectively.[43] For $CdSmGaB_2O_7$, there is a strong absorption band below 300 nm with maxima at about 224 nm, which is mainly ascribed to the ligand (O^{2-}) to metal charge transfer (CT) transition. In the region between 300 and 500 nm, a series of sharp absorption peaks were observed at about 317, 346, 363, 377, 405, 418, 444, 465, 472, and 483 nm, which can be assigned to the $^6H_{5/2} \rightarrow {}^4F_{11/2}$, $^6H_{5/2} \rightarrow {}^3H_{7/2}$, $^6H_{5/2} \rightarrow {}^4F_{9/2}$, $^6H_{5/2} \rightarrow {}^4D_{5/2}$, $^6H_{5/2} \rightarrow {}^4K_{11/2}$, $^6H_{5/2} \rightarrow {}^4M_{19/2}$, $^6H_{5/2} \rightarrow {}^4G_{9/2} + {}^4I_{15/2}$, $^6H_{5/2} \rightarrow {}^4F_{5/2}$, $^6H_{5/2} \rightarrow {}^4I_{11/2}$, $^6H_{5/2} \rightarrow {}^4M_{15/2}$ transitions, respectively, as found in the PLE spectrum [Fig. 4(b)].[44,45]

The optical band gap (E_g) can be estimated with the help of Tauc's relation:[46]

$$\alpha h\nu = A(h\nu - E_g)^n$$

where α, h, ν, A and E_g stand for absorption coefficient, Planck's constant, light frequency, proportionality constant and band gap, respectively. n is a constant related to the transition ($n = 1/2$ and 2 for direct and indirect allowed transitions, respectively). If the absorption coefficient α is replaced by the absorbance obtained from the UV-vis spectrum, $(\alpha h\nu)^{1/n}$ is plotted against the photon energy ($h\nu$), and on this basis, a line tangent to the inflection point of the curve is further drawn, the intercept of the tangent to the x-axis will give a good approximation of the band gap energy. In the present case, the indirect and direct

band gaps are estimated to be 4.10 and 4.33 eV for $CdTbGaB_2O_7$, whereas they are 3.82 (indirect) and 4.87 eV (direct) for $CdSmGaB_2O_7$, respectively, as shown in the insets of Fig. S3.† These bandgap values are similar to those previously reported in other Tb- and Sm-containing borates, such as $K_3Li_3Tb_7(BO_3)_9$ [4.19 (indirect) and 4.55(direct) eV] and $K_3Sm_3(BO_3)_4$ [4.99 (direct) eV].[47,48]

3.4. Phase purity and morphology

In order to check the correctness of the single-crystal structure, additional Rietveld refinements of powder XRD data from $CdTb_{1-x}Sm_xGaB_2O_7$ ($x = 0$ and 1) were carried out using TOPAS software.[49] In the refining process, the single-crystal data of the Tb phase were employed as the initial model, a total of 51 parameters were refined, including 47 profile and 4 structure ones. The final refinement patterns are depicted in Fig. 2(a) and (b), where the low R-factors and the small differences between the measured and calculated data were obtained, indicating good fitting quality and high phase purity. Although the cell dimensions of $CdTbGaB_2O_7$ from Rietveld refinements [$a = b = 7.3437(1)$ Å, $c = 4.7201(1)$ Å, and $V = 254.558(8)$ Å^3] are somewhat smaller than the single-crystal data [Table 1], their relative deviations are less than 0.5%, revealing that the determined structure should be quite credible.

Powder XRD patterns of the as-prepared $CdTb_{1-x}Sm_xGaB_2O_7$ ($0 \leq x \leq 1$) samples are presented in Fig. 2(c). All experimental diagrams agree well with the simulated pattern of $CdTbGaB_2O_7$, indicating that doping of Sm^{3+} ions did not generate any distinct impurity or induce significant changes in the host structure. In addition, the enlargement of the reflections in the range of $2\theta = 32.8°$–$33.4°$ is shown in the right part of Fig. 2(c), where a continuous left-shift of the representative peak (121) can be clearly observed with increasing Sm^{3+} content in $CdTb_{1-x}Sm_xGaB_2O_7$. In fact, as we discussed earlier, Cd and Tb atoms in $CdTbGaB_2O_7$ are statistically distributed over one atomic site, and each (Cd/Tb) is surrounded by eight oxygen atoms, forming a distorted (Cd/Tb)O$_8$ polyhedron, while Ga and B atoms are completely ordered and tetrahedrally coordinated with oxygen atoms. Considering the ionic radii and coordination number (CN) of Cd^{2+} (1.10 Å, CN = 8), Tb^{3+} (1.040 Å, CN = 8), Sm^{3+} (1.079 Å, CN = 8), Ga^{3+} (0.47 Å, CN = 4) and B^{3+} (0.11 Å, CN = 4),[23] it is reasonable to believe that the doped Sm^{3+} ions will replace Tb^{3+} and occupy (Cd/Tb) sites randomly in the host, which will lead to lattice expansion, thus shifting the diffraction peaks to smaller 2θ values according to the Bragg equation.

The ionic radii for eightfold coordinated Tb^{3+} and Sm^{3+} differ only by 3.75% and both fully concentrated Tb^{3+} and Sm^{3+} compounds are isostructural. Therefore, it is expected that there is a solid solution series whose lattice constants are linearly related to the Sm^{3+}/Tb^{3+} ratio. In order to confirm this point, Rietveld refinements of powder XRD profiles were also performed on $CdTb_{1-x}Sm_xGaB_2O_7$ ($x = 0.001, 0.002, 0.005, 0.01, 0.05, 0.1$ and 0.2), as shown in Fig. S4.† For these refinements, the atomic coordinates of Ga, B and O sites, atomic occupancies, and isotropic thermal displacement factors were fixed, while the atomic coordinates of the (Cd/Tb/Sm) site and cell
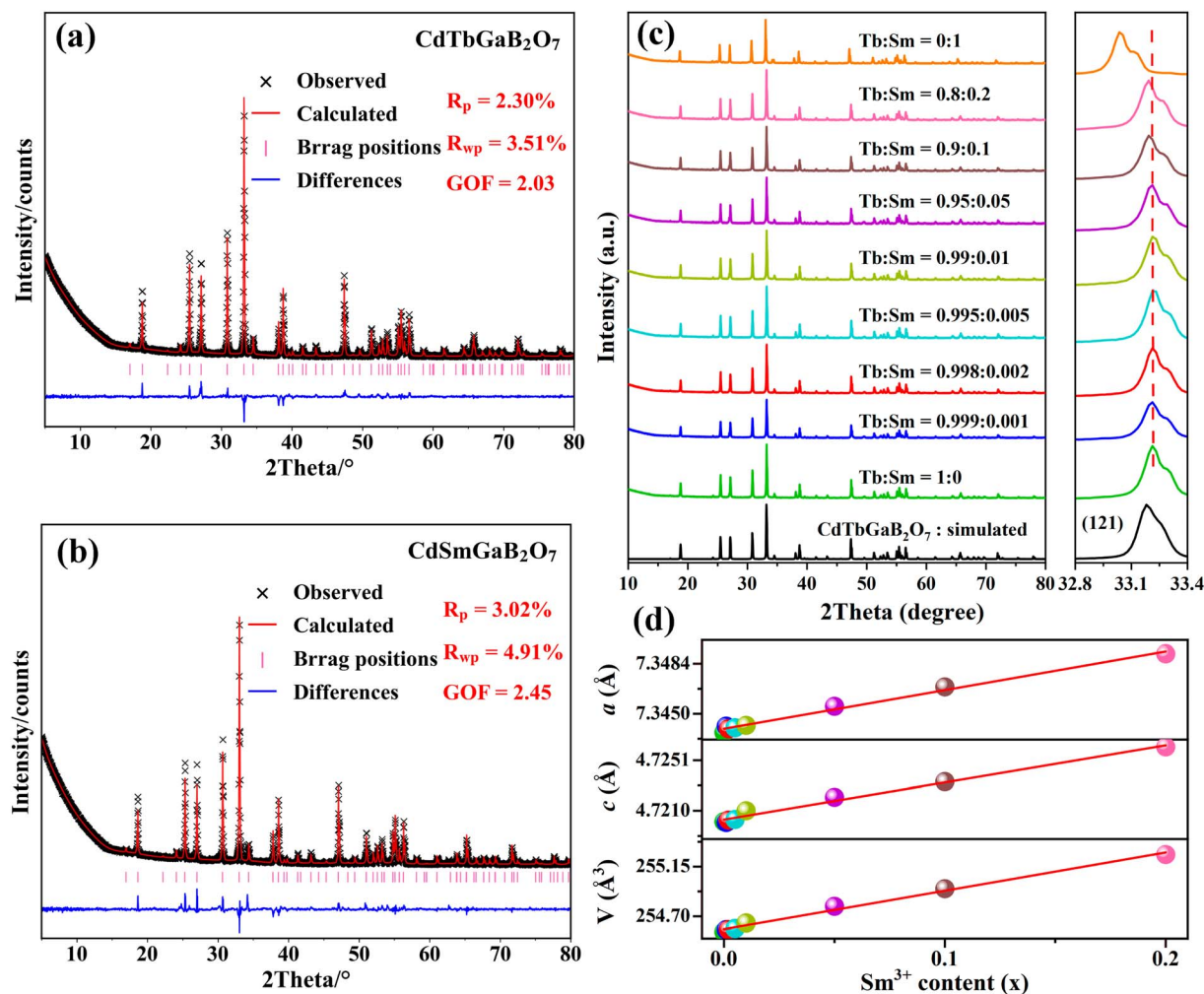
Fig. 2 (a and b) Rietveld refinements of the XRD files for $CdTb_{1-x}Sm_xGaB_2O_7$ ($x = 0$ and 1). (c) XRD patterns of the $CdTb_{1-x}Sm_xGaB_2O_7$ ($0 \leq x \leq 1$) phosphors. (d) The cell parameters (a, c, and V) obtained by Rietveld refinements against the Sm^{3+} concentration (x).

parameters were refined along with other parameters. The lattice parameters and atomic coordinates of all species obtained from Rietveld fitting are summarized in Tables S5 and S6,† while the lattice parameters for $0 \leq x \leq 0.2$ were plotted as a function of the dopant Sm^{3+} concentration (x) in Fig. 2(d). Obviously, cell parameters, including axis lengths (a and c) and volume (V), increase linearly with the incorporation of Sm^{3+}, as predicted by Vegard law. This phenomenon can be explained by the larger ionic radius of Sm^{3+} compared to that of Tb^{3+}, which is strong evidence of the successful cationic substitution.

The SEM images of the representative phosphor $CdTb_{0.995}$-$Sm_{0.005}GaB_2O_7$ are illustrated in Fig. 3. The particles exhibit irregular shapes in the agglomerated form with several microns in size. They are typical products prepared by the high-temperature solid state reaction. Besides, the EDX spectrum reveals that in addition to Au as a coating element, there are expected elements in the studied sample, including Cd, Tb, Sm, Ga and O (B is too light to be detected). The elemental mappings demonstrate that all constituent elements are evenly distributed among the selected particle. Hence, the successful doping

of Sm^{3+} into the $CdTbGaB_2O_7$ matrix to form a homogenous phase can be verified based on the XRD and EDX results.

3.5. XPS spectra

XPS was performed to determine the surface chemical components of the phosphor $CdTb_{0.995}Sm_{0.005}GaB_2O_7$. Fig. S5(a)† depicts a typical survey scan in the range of 1350–0 eV, which contains Cd 3p, 3d, 4d, Tb 3d, 4d, Ga 2p, 3d, B 1s, O 1s and C 1s core levels along with Ga and O Auger peaks, confirming the sample composition. The presence of C can be ascribed to the expected adsorption of adventitious carbon from XPS instrument itself, and the C 1s peak of 284.6 eV was used as a standard to adjust other peaks. To further inspect the chemical state of each element, narrow scan XPS measurements were done, and the results are shown in Fig. S5(b)–(g).† One can see that there are two distinct peaks at 411.62 and 404.79 eV in Fig. S5(b),† which are assigned to Cd $3d_{3/2}$ and $3d_{5/2}$ core levels, and can be used as a fingerprint to identify the existence of Cd^{2+}.[50] The Tb 3d XPS spectrum is depicted in Fig. S5(c),† where two strong peaks associated with Tb $3d_{3/2}$ and $3d_{5/2}$ were clearly observed at
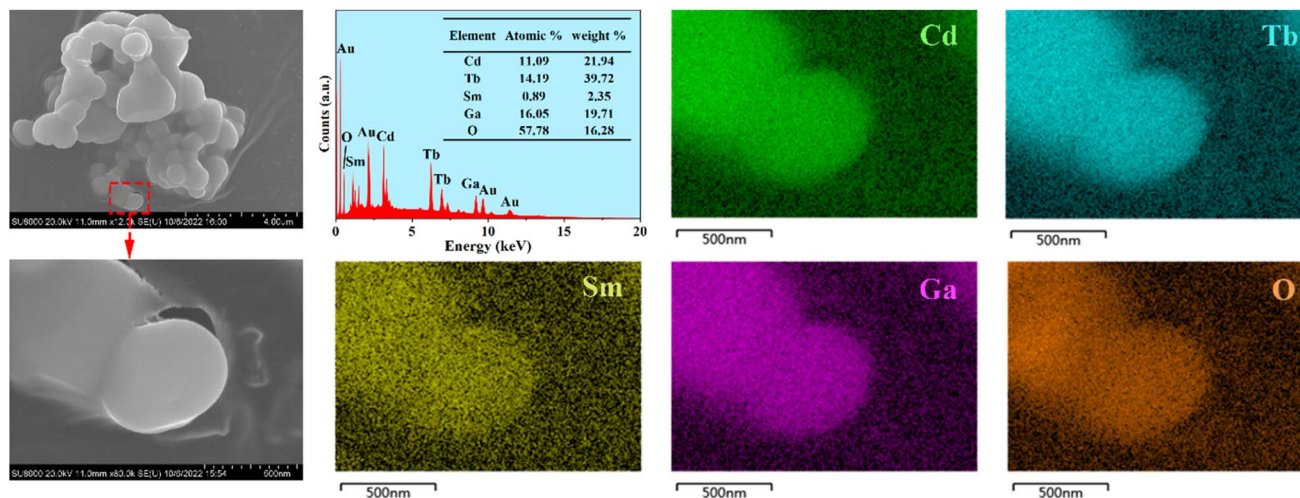
Fig. 3 FE-SEM images, typical EDS results, and elemental mapping of the CdTb$_{0.995}$Sm$_{0.005}$GaB$_2$O$_7$ phosphor. Note that a thin layer of Au was evaporated on the sample surface to provide conductivity prior to SEM inspection.

1278.71 and 1243.76 eV. These binding energies and their differences confirm the +3 valence state of Tb in the doped system.[51] In Fig. S5(d),† although the Sm 4d XPS signal is relatively weak because of the very low dopant concentration in the phosphor, it can be deconvoluted into three components, corresponding to Sm 4d$_{3/2}$ (~134.29 eV), 4d$_{5/2}$ (~130.98 eV) and a satellite peak (127.87 eV), respectively, similar to the earlier results obtained for β-RbSm(MoO$_4$)$_2$.[52] This indicates that the doped Sm element predominantly maintains the state of Sm^{3+} in the CdTbGaB$_2$O$_7$ matrix. Furthermore, the Ga 3p spectrum is composed of doublet components at 108.58 eV (Ga 3p$_{1/2}$) and 104.96 eV (Ga 3p$_{3/2}$) with the spin–orbit splitting of ~3.62 eV, indicating that Ga appears as +3 valence.[53] The B 1s spectrum was fitted to a single peak, which is attributed to the B atoms bonded to oxygen atoms (B–O) in borates, and its binding energy of 191.57 eV is in good accord with the literature report.[54] The O 1s spectrum can be resolved into two components, of which the main peak at 530.95 eV usually denotes the presence of structural oxide (O^{2-}), while the shoulder peak at 532.77 eV corresponds to the oxygen in adsorbed water (H$_2$O) at the sample surface.[55] No other impurity peaks have been identified from the XPS spectra, supporting the aforementioned XRD and EDX analyses. All these observations ensure the successful cationic substitution, after which a systematic investigation of the photoluminescence properties of the CdTb$_{1-x}$Sm$_x$GaB$_2$O$_7$ phosphors was conducted.

3.6. PLE and PL spectra

Fig. 4(a) shows the typical photoluminescence excitation (PLE) and emission (PL) spectra of the CdTbGaB$_2$O$_7$ phosphor. The PLE spectrum obtained by monitoring 545 nm emission (Tb^{3+}: $^5D_4 \rightarrow {}^7F_5$) consists of two strong broad bands below 300 nm, along with many sharp peaks in the higher wavelength region. The strong broadband centered at ~248 and 286 nm can be attributed to the spin-allowed ($^7F_6$–^7D_J) and spin-forbidden ($^7F_6$–^9D_J) 4f^8 $\rightarrow$ 4f^{7}5d^1 inter-configurational Tb^{3+} transitions, respectively.[56] The other excitation peaks appearing at 318, 343,

352, 370, 377, and 485 nm correspond to the parity- and spin-forbidden 4f–4f transitions of the Tb^{3+} ion, that is, from the $^7F_6$ ground state to the excited states of $^5D_0$, $^5L_6$, $^5L_8$, $^5L_{10}$, $^5D_3$, and $^5D_4$ levels, as labelled in Fig. 4(a).[43] The PL spectrum recorded under the excitation of 370 nm gives four sets of characteristic optical transitions of Tb^{3+}, namely $^5D_4 \rightarrow {}^7F_J$ (J = 6, 5, 4, and 3) at approximately 491, 545, 587 and 623 nm, respectively. The transition of $^5D_4 \rightarrow {}^7F_5$ at ~545 nm is the most prominent, which explains the strong green emission of CdTbGaB$_2$O$_7$. As expected, no emission coming from $^5D_3$ level has been observed due to the fast cross relaxation processes [Tb^{3+} ($^5D_3$) + Tb^{3+} ($^7F_6$) $\rightarrow$ Tb^{3+} ($^5D_4$) + Tb^{3+} ($^7F_0$)] present in fully concentrated terbium materials.[57]

The PLE and PL spectra of the CdSmGaB$_2$O$_7$ phosphor are presented in Fig. 4(b). The PLE spectrum monitored with 603 nm emission exhibits a broadband near 250 nm together with multiple sharp peaks at 319, 346, 362, 377, 405, 440, 474, 502 and 528 nm, which are associated with the O$^{2-} \rightarrow$ Sm^{3+} charge–transfer transition and the characteristic Sm^{3+} f–f transitions: $^6H_{5/2} \rightarrow {}^4F_{11/2}$, $^6H_{5/2} \rightarrow {}^3H_{7/2}$, $^6H_{5/2} \rightarrow {}^4F_{9/2}$, $^6H_{5/2} \rightarrow {}^4D_{5/2}$, $^6H_{5/2} \rightarrow {}^4K_{11/2}$, $^6H_{5/2} \rightarrow {}^4G_{9/2}$, $^6H_{5/2} \rightarrow {}^4I_{11/2}$, $^6H_{5/2} \rightarrow {}^4G_{7/2}$ and $^6H_{5/2} \rightarrow {}^4F_{3/2}$, respectively.[44,45] The presence of the intense absorption bands from 350 to 490 nm suggests that CdSmGaB$_2$O$_7$ can be used as a potential phosphor for UV/NUV LED lighting. When the phosphor is exposed to 405 nm radiation, it emits luminescence at about 564, 603, 646, and 705 nm, assigned to the $^4G_{5/2} \rightarrow {}^6H_J$ (J = 5/2, 7/2, 9/2, 11/2) transitions of Sm^{3+}, respectively. Among them, $^4G_{5/2} \rightarrow {}^6H_{5/2}$ and $^4G_{5/2} \rightarrow {}^6H_{9/2}$ are purely magnetic dipole (MD) and electric dipole (ED) allowed transitions, respectively, while $^4G_{5/2} \rightarrow {}^6H_{7/2}$ is a MD allowed one but also ED dominated. Generally speaking, the integral intensity ratio of the ED/MD transitions [R = I($^4G_{5/2} \rightarrow {}^6H_{9/2}$)/I($^4G_{5/2} \rightarrow {}^6H_{5/2}$)] is used to assess the symmetry nature of trivalent 4f ions. In this work, the R value was calculated as 1.45 (>1), implying that Sm^{3+} ions are located in the low symmetry sites. In fact, our structural analysis reveals that Sm^{3+} will replace Tb^{3+} and share the Wyckoff
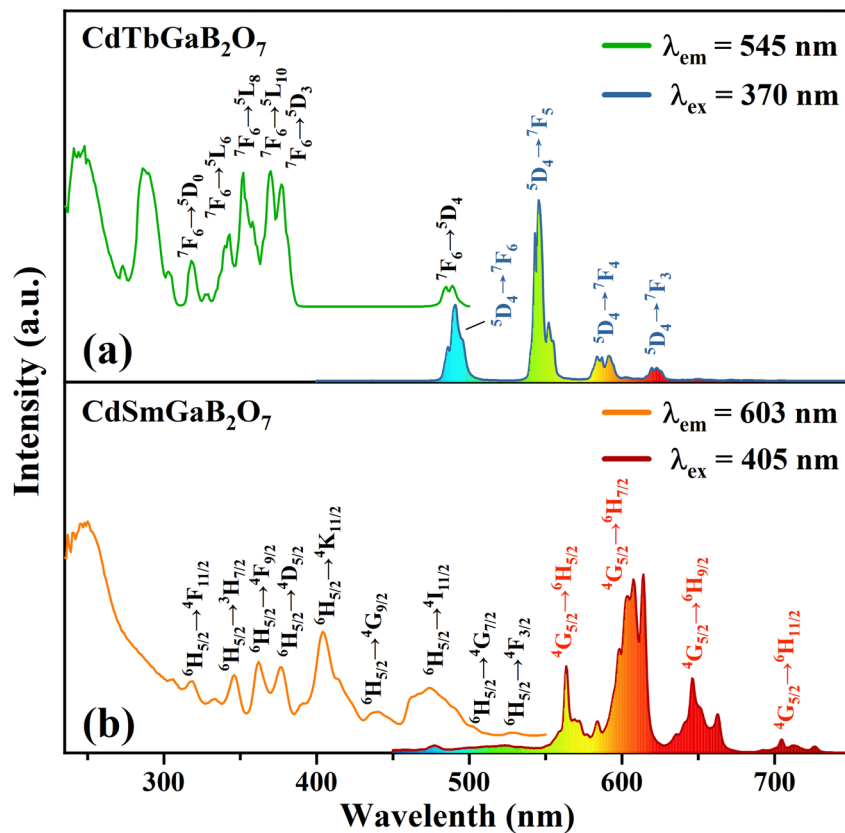
Fig. 4 The PLE and PL spectra of $CdTbGaB_2O_7$ (a) and $CdSmGaB_2O_7$ (b).

4e site with Cd^{2+}, which is on a mirror plane without inversion center, as shown in Table S1† and Fig. 1(c).

The PLE spectra of the $CdTb_{1-x}Sm_xGaB_2O_7$ phosphors with different Sm^{3+} concentrations are shown in Fig. 5(a) and (b). By monitoring the Tb^{3+} emission at 545 nm ($^5D_4 \rightarrow {}^7F_5$), the PLE spectra show the f–d and f–f transitions of Tb^{3+} and the excitation intensity decreases remarkably and steadily towards a higher Sm^{3+} content and finally becomes negligible at $x = 0.2$, suggesting the presence of efficient $Tb^{3+} \rightarrow Sm^{3+}$ energy transfer. It is noteworthy that Sm^{3+} excitation peaks were undetectable in each case, which ascertains the fact that there was no possibility of energy transfer from Sm^{3+} to Tb^{3+}. On the other hand, the PLE spectra monitored with the 603 nm emission (Sm^{3+}: $^4G_{5/2} \rightarrow {}^6H_{7/2}$) contain not only the characteristic excitation peak of Sm^{3+} at 405 nm, but also those of Tb^{3+} originated from f–d and f–f transitions, with the latter dominating the PLE spectra, which further confirms the efficient $Tb^{3+} \rightarrow Sm^{3+}$ energy transfer. Besides, the intensities of the Tb^{3+} excitation transitions (*e.g.*, $^7F_6-{}^5L_{10}$ at 370 nm) successively increase with increasing Sm^{3+} concentration up to $x = 0.005$ and then decrease, implying the occurrence of concentration quenching at $x > 0.005$.

The influence of Sm^{3+} content on the PL spectra of $CdTb_{1-x}Sm_xGaB_2O_7$ were also studied, as shown in Fig. 5(c) and (d). As expected, upon excitation at 370 nm (Tb^{3+}: $^7F_6 \rightarrow {}^5L_{10}$), $CdTbGaB_2O_7$ displays only the characteristic emissions of Tb^{3+}. With the doping of Sm^{3+} ions, besides Tb^{3+} emissions at 491 ($^5D_4 \rightarrow {}^7F_6$) and 545 nm ($^5D_4 \rightarrow {}^7F_5$), the characteristic

emissions of Sm^{3+} at 603 nm ($^4G_{5/2} \rightarrow {}^6H_{7/2}$) and 646 nm ($^4G_{5/2} \rightarrow {}^6H_{9/2}$) can also be observed. Furthermore, as the Sm^{3+} concentration increases, the emission intensity of Tb^{3+} at 545 nm first decreases rapidly, and then remains at a relative low value with little difference, as illustrated in the inset of Fig. 5(c). At the same time, the emission intensity of Sm^{3+} at 603 nm increases initially until the Sm^{3+} concentration reaches $x = 0.005$, reflecting the result of energy transfer from Tb^{3+} to Sm^{3+}. However, once the Sm^{3+} content is further increased to beyond $x = 0.005$, the concentration quenching occurs between Sm^{3+} ions, resulting in a decrease in the emission intensity. In addition, the PL spectra under direct excitation of the Sm^{3+} 4f levels at 405 nm (Sm^{3+}: $^6H_{5/2} \rightarrow {}^4K_{11/2}$) yield only the emission peaks of Sm^{3+} and not those of Tb^{3+}, further confirming the absence of energy transfer from Sm^{3+} to Tb^{3+}. In this case, the emission intensity of Sm^{3+} first increases until $x = 0.05$ and then appears a downfall, which is consistent with the trend of Sm^{3+} characteristic excitation peak at 405 nm in the PLE spectra monitored at 603 nm emission of Sm^{3+} [Fig. 5(b)]. However, it is different from the situation observed in the 370 nm indirect excitation *via* the energy transfer from Tb^{3+} to Sm^{3+}, where the optimal Sm^{3+} doped content is $x = 0.005$. As everyone knows, the PL spectrum is strongly affected by the excitation wavelength.[58] The fact that indirect and direct excitation leads to different quenching concentrations has already been reported in some other phosphors, such as $Ba_3BiPbY_{1-x}Eu_xO(BO_3)_4$, $CeO_2 : Eu^{3+}$ and $SnO_2 : Eu^{3+}$.[59–61]
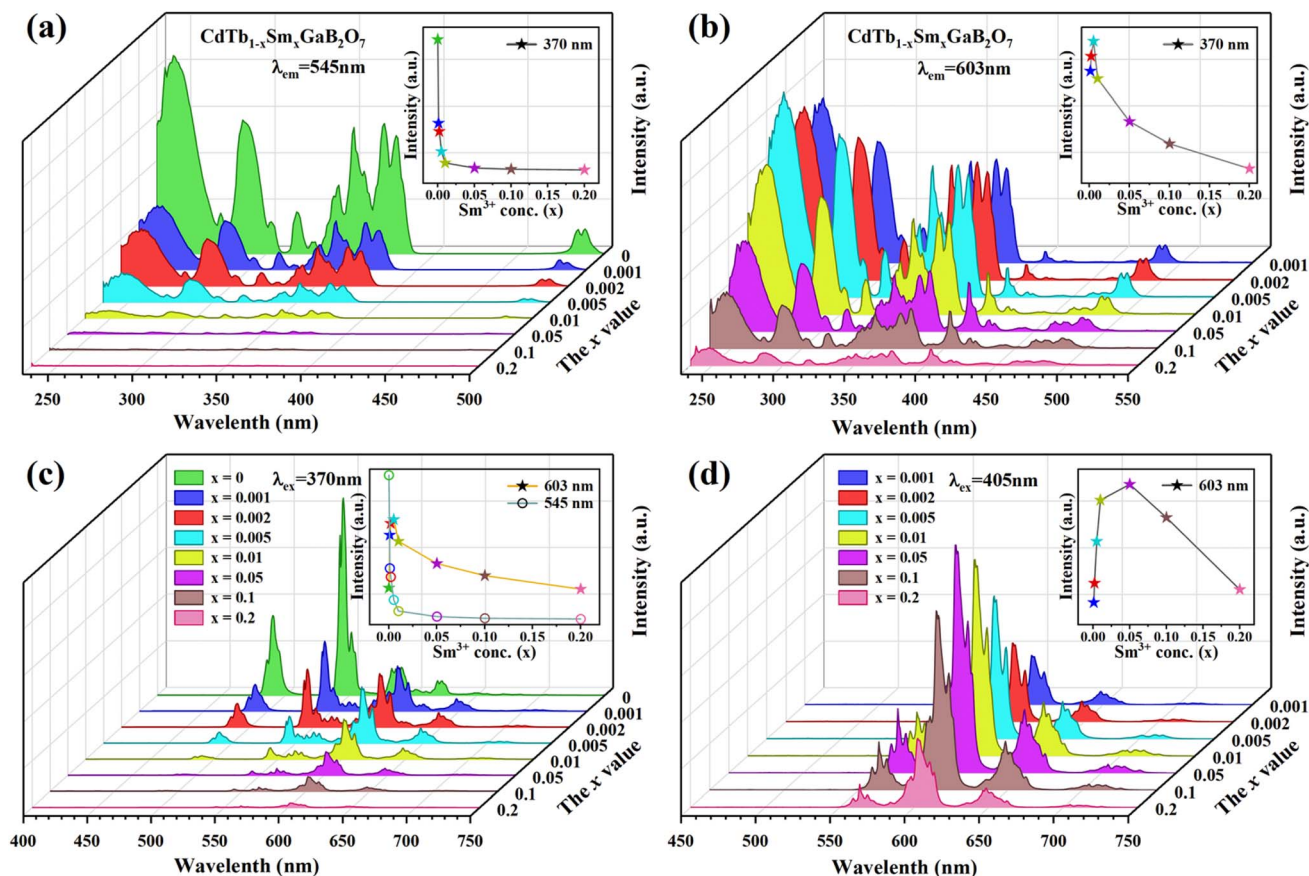
Fig. 5 The concentration dependent PLE [(a) λ_{em} = 545 nm; (b) λ_{em} = 603 nm] and PL [(c) λ_{ex} = 370 nm; (d) λ_{ex} = 405 nm] spectra of the CdTb$_{1-x}$Sm$_x$GaB$_2$O$_7$ fluorescent powders.

3.7. Fluorescence lifetime and energy transfer mechanism

To further illustrate the Tb^{3+} → Sm^{3+} energy transfer process, the Tb^{3+} luminescence decay curves of the CdTb$_{1-x}$Sm$_x$GaB$_2$O$_7$ phosphors (λ_{ex} = 370 nm, λ_{em} = 545 nm) were recorded, as shown in Fig. 6. All curves show a second-order exponential decay, which can be fitted by the following equation:

$$I_t = I_0 + B_1 \exp\left(-\frac{t}{\tau_1}\right) + B_2 \exp\left(-\frac{t}{\tau_2}\right)$$

where I_0 and I_t are the luminescence intensities corresponding to time 0 and t, B_1 and B_2 are fitting parameters, and τ_1 and τ_2 are lifetimes for rapid and slow decays, respectively. The double-exponential behavior indicates a heterogeneous distribution of Tb^{3+} ions in the CdTb$_{1-x}$Sm$_x$GaB$_2$O$_7$ phosphors. In fact, when the excitation energy is transferred from the donor (Tb^{3+}) to acceptor (Sm^{3+}), a double-exponential decay behavior of the activator is usually observed.[17] The decay process is characterized by an average lifetime (τ_{avg}), which can be calculated as follows:

$$\tau_{avg} = \frac{B_1\tau_1^2 + B_2\tau_2^2}{B_1\tau_1 + B_2\tau_2}$$

The τ_{avg} values determined for different Sm^{3+} concentrations are also shown in Fig. 6. Apparently, the luminescence lifetime

of Tb^{3+} in CdTb$_{1-x}$Sm$_x$GaB$_2$O$_7$ decreases successively with the increase of Sm^{3+} concentration, which offers clear evidence for the energy transfer from Tb^{3+} to Sm^{3+}. The energy transfer efficiency (η) from sensitizer to activator can be evaluated with the following expression:

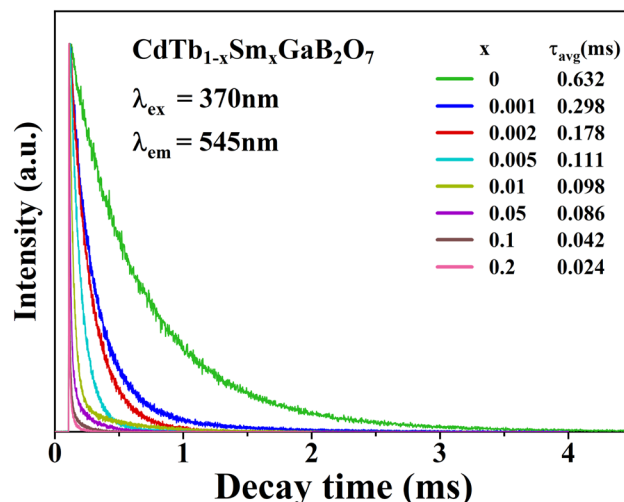**Fig. 6** Tb^{3+} decay curves of the CdTb$_{1-x}$Sm$_x$GaB$_2$O$_7$ ($0 \leq x \leq 0.2$) phosphors monitoring 545 nm emission.

Table 2 CIE chromaticity coordinates, CCT values and energy transfer efficiencies (η) of the $CdTb_{1-x}Sm_xGaB_2O_7$ ($0 \leq x \leq 0.2$) phosphors

$CdTb_{1-x}Sm_xGaB_2O_7$	λ_{ex} (nm)	CIE (x, y)	CCT (K)	η (%)
1 $x = 0$	370	(0.3134, 0.5750)	5854	—
2 $x = 0.001$	370	(0.4384, 0.4957)	3574	52.85
3 $x = 0.002$	370	(0.4656, 0.4779)	3093	71.84
4 $x = 0.005$	370	(0.5213, 0.4430)	2227	82.44
5 $x = 0.01$	370	(0.5539, 0.4202)	1838	84.49
6 $x = 0.05$	370	(0.5739, 0.4044)	1677	86.39
7 $x = 0.1$	370	(0.5746, 0.3979)	1655	93.35
8 $x = 0.2$	370	(0.5391, 0.3798)	1706	96.20

$$\eta = 1 - \left(\frac{\tau}{\tau_0}\right)$$

where τ and τ_0 are the decay times of Tb^{3+} ($^5D_4 \rightarrow {}^7F_5$) with and without Sm^{3+} co-doping. The calculated η values are provided in Table 2. It is found that the energy transfer efficiency increases monotonously from 52.85% to 96.20% with the raising Sm^{3+} concentration from $x = 0.001$ to 0.2.

Fig. 7 shows the energy level diagrams of Tb^{3+} and Sm^{3+} ions illustrating the energy migration processes in $CdTb_{1-x}Sm_x$-GaB_2O_7. Upon excitation at 370 nm, the electrons on Tb^{3+} ions can jump from the $^7F_6$ ground state to the $^5L_{10}$ excited state. Afterwards, the nonradiative transition (NR) took place, leading to the population of the $^5D_4$ level. While some of the excited electrons return to the $^7F_{6,5,4,3}$ ground state level in a radiative

manner, generating the typical Tb^{3+} emissions. The remaining electrons at the $^5D_4$ level of Tb^{3+} can move to the $^4G_{7/2}$ excited level of Sm^{3+} due to energy level matching, followed by nonradiative relaxation to the $^4G_{5/2}$ excited state and then radiative relaxation to the ^6H_J ($J = 5/2$, 7/2, 9/2, 11/2) ground states to produce the observed Sm^{3+} emissions. This process enhances the characteristic emission of Sm^{3+} and simultaneously reduces the fluorescence emission intensity of Tb^{3+}. In addition, it can be seen from Fig. 4(a) and (b) that there is a significant spectral overlap between the emission band of Tb^{3+} and the excitation band of Sm^{3+} in the range of 475–525 nm, which indicates that the energy transfer from Tb^{3+} to Sm^{3+} can be anticipated in $CdTb_{1-x}Sm_xGaB_2O_7$ via $^5D_4$ channel: $^5D_4$ (Tb^{3+}) + $^6H_{5/2}$ (Sm^{3+}) $\rightarrow {}^7F_6$ (Tb^{3+}) + $^4I_{11/2}$ (Sm^{3+}).[62] The $Tb^{3+} \rightarrow Sm^{3+}$ energy transfer is almost irreversible because the $^5D_4$ level of Tb^{3+} is slightly higher than the $^4G_{7/2}$ level of Sm^{3+}, which also explains the observation that Tb^{3+} cannot be excited by 405 nm ($Sm^{3+}:{}^6H_{5/2} \rightarrow {}^4K_{11/2}$ transition) in this system.

3.8. Emitting light color analysis

The CIE coordinates and CIE chromaticity diagram for the samples $CdTb_{1-x}Sm_xGaB_2O_7$ ($0 \leq x \leq 0.2$) were measured, as shown in Table 2 and Fig. 8. The inset of Fig. 8 also shows the digital photos of the selected phosphors under a 370 nm UV lamp. One can see that the $CdTbGaB_2O_7$ host emits green light when excited at 370 nm. Once Sm^{3+} ions were doped into this host and the Sm^{3+} content changed from $x = 0$ to 0.1, the CIE coordinates of $CdTb_{1-x}Sm_xGaB_2O_7$ would vary almost linearly
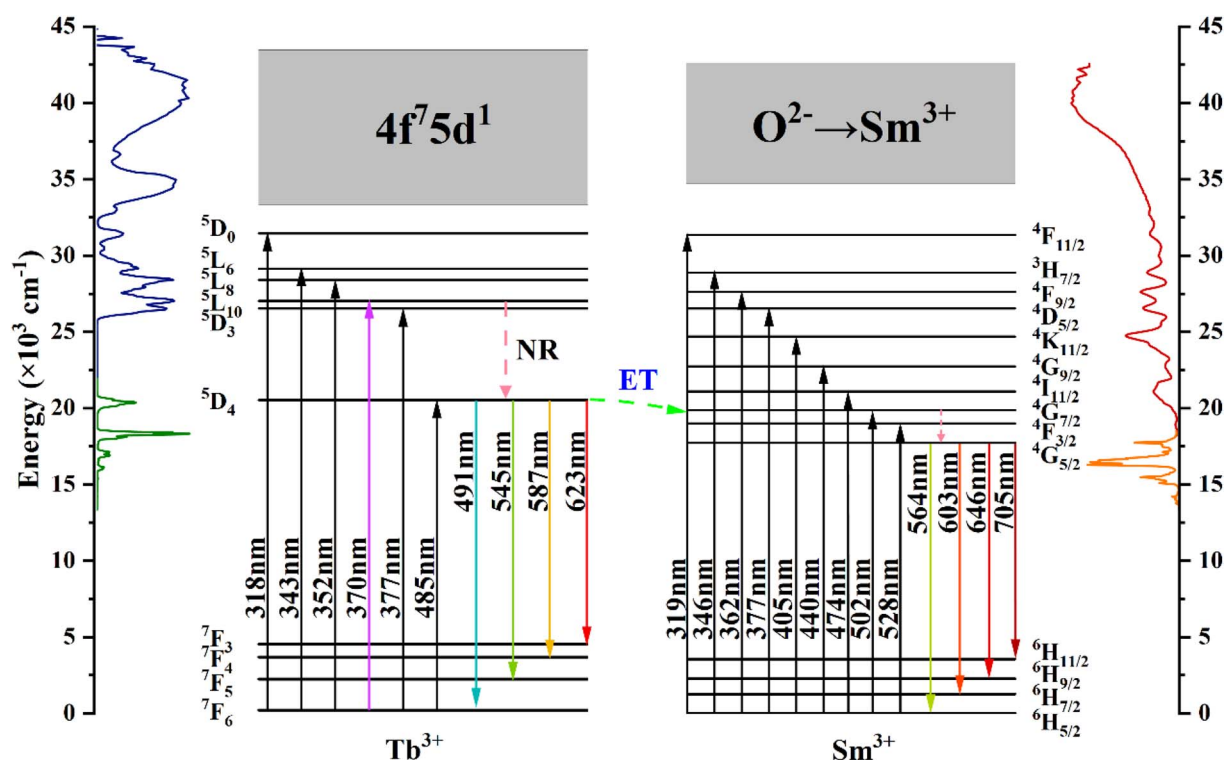
Fig. 7 Schematic energy-level diagrams of Tb^{3+} and Sm^{3+} in $CdTb_{1-x}Sm_xGaB_2O_7$, showing energy-transfer process (ET: energy transfer; NR: nonradiative).
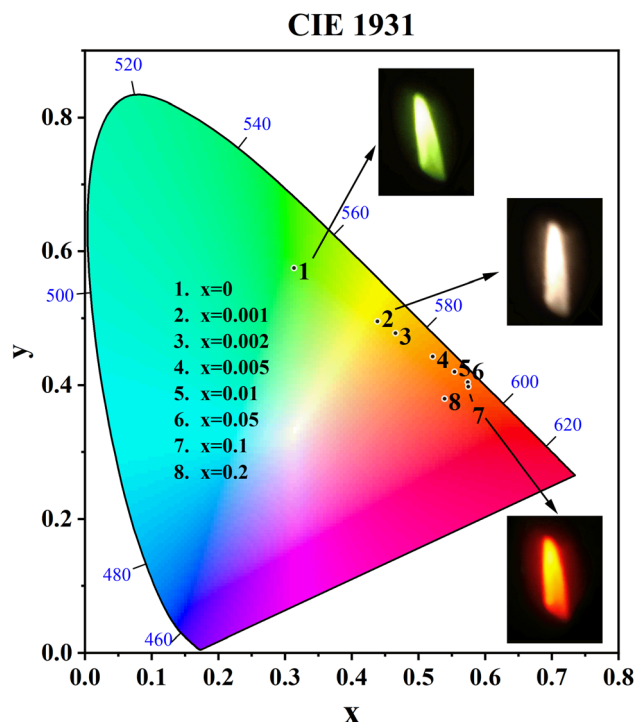
Fig. 8 CIE chromaticity coordinates of the CdTb$_{1-x}$Sm$_x$GaB$_2$O$_7$ ($x = 0$, 0.001, 0.002, 0.005, 0.01, 0.05, 0.1, 0.2) phosphors and digital photographs of the selected samples ($x = 0$, 0.001 and 0.1) ($\lambda_{ex} = 370$ nm).

from (0.3134, 0.5750) to (0.5746, 0.3979), which means that the emitting color changes continuously from green to orange-red. In addition, as seen from Fig. 5(c), when the Sm^{3+} content was further increased from $x = 0.1$ to 0.2, the characteristic blue and green emissions of Tb^{3+} remained basically unchanged, while the orange and red emissions of Sm^{3+} were significantly reduced due to the concentration quenching effect. Therefore, the chromaticity coordinates of the $x = 0.2$ sample are shifted toward the blue direction with respect to the $x = 0.1$ sample. A similar phenomenon was found in some previously reported Tb^{3+} and Sm^{3+} codoped phosphors, such as Y$_3$Al$_2$Ga$_3$O$_{12}$: 0.5Tb^{3+}, ySm^{3+}, Na$_3$Bi(PO$_4$)$_2$: 0.1Tb^{3+}, xSm^{3+} and LaAl$_{2.03}$B$_4$O$_{10.54}$: 0.1Tb^{3+}, ySm^{3+}.[62-64] Next is the CCT (the Correlated Color Temperature), which is a measure of how cool or warm the appearance of a light source will be.[65] The CCT can be calculated by the analytical equation proposed by McCamy:[66]

$$CCT = -449n^3 + 3525n^2 - 6823.3n + 5520.33$$

where $n = (x - x_e)/(y - y_e)$ and ($x_e = 0.332$, $y_e = 0.186$). The obtained CCT values for the CdTb$_{1-x}$Sm$_x$GaB$_2$O$_7$ ($0.001 \leq x \leq 0.2$) phosphors decrease with the enhancement of Sm^{3+} concentration and are in the range of 1655–3574 K (Table 2), which means that the prepared phosphors have the "neutral to warm" colors. The above results indicate that multicolor photoluminescence can be realized in CdTb$_{1-x}$Sm$_x$GaB$_2$O$_7$ by controlling Sm^{3+} doping amount and choosing the appropriate excitation wavelength, and this material has potential application prospects as a color-tunable phosphor for w-LEDs.

3.9. Quantum yield and thermal stability

Quantum yield (QY) serves as a critical parameter to evaluate the luminescence properties of phosphors, which can be measured based on the following equation:

$$QY = \frac{\int L_S}{\int E_R - \int E_S}$$

where $\int L_S$ is the integrated emission profile of the sample, $\int E_R$ and $\int E_S$ represent the integrated excitation profile without and with the sample in the integrating sphere, respectively. The excitation and emission spectra of the phosphor CdTb$_{0.995}$-Sm$_{0.005}$GaB$_2$O$_7$ and the reference sample collected in an integrating sphere ($\lambda_{ex} = 370$ nm) are displayed in Fig. S6,† which shows a QY of ~13.22%. The relatively low QY may be due to the severe aggregation of phosphor particles. We believe that higher QY could be obtained by controlling the particle size, size distribution, morphology and crystalline defects *via* optimization of the preparation conditions or exploration of alternative synthetic routes. This will be investigated in our future work.

Thermal stability is one of the most important prerequisites for the synthesized phosphor to be used in a LED, as temperature greatly affects the brightness and color output. Fig. 9(a) exhibits the temperature-dependent PL spectra of the CdTb$_{0.995}$Sm$_{0.005}$GaB$_2$O$_7$ sample upon 370 nm excitation. Obviously, the position and shape of emission peaks remain almost unchanged, while the emission intensity diminishes with increasing temperature due to thermal quenching caused by non-radiative transitions. Furthermore, the emission intensities are integrated over the spectral range of 450–750 nm, and are normalized as compared to the case of 303 K. The results in the inset of Fig. 9(a) show that the relative emission intensity of CdTb$_{0.995}$Sm$_{0.005}$GaB$_2$O$_7$ at 423 K (the temperature at which LEDs typically operate) remains about 94% of that at 303 K. Compared with some previously reported phosphors, such as Ba$_3$BiPbEuO(BO$_3$)$_4$ (37%), Ba$_2$Lu$_{4.48}$Eu$_{0.5}$La$_{0.02}$B$_5$O$_{17}$ (38.2%) and LaMgAl$_{11}$O$_{19}$: 0.05Sm^{3+}, 0.2Eu^{3+} (<60%),[59,67,68] the thermal stability of CdTb$_{0.995}$Sm$_{0.005}$GaB$_2$O$_7$ seems to be better. For further understanding the influence of temperature on luminescence, the activation energy of thermal quenching (ΔE) was measured on the basis of the modified Arrhenius equation[69]:

$$I = \frac{I_0}{1 + A \exp\left(-\dfrac{\Delta E}{kT}\right)}$$

where I and I_0 are related to the PL intensity at a given temperature T and initial temperature, respectively, A is a constant for the host, and k stands for the Boltzmann coefficient (8.62×10^{-5} eV K^{-1}). Upon specific rearrangement, the above equation can be rewritten as:

$$\ln\left(\frac{I_0}{I} - 1\right) = -\frac{\Delta E}{kT} + \ln A$$

Fig. 9(b) shows the relationship between $\ln[(I_0/I) - 1]$ and $1/kT$ of the phosphor. It can be seen that the plot can be well fitted to a straight line with the correlation coefficient $R^2 = 0.972$ and
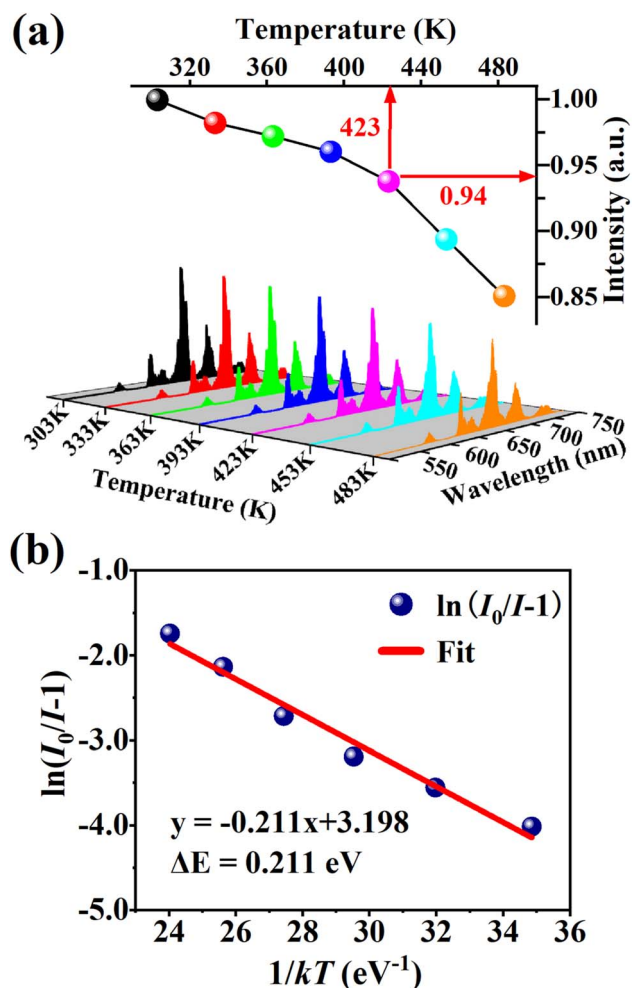
Fig. 9 (a) PL spectra and normalized PL intensities of CdTb$_{0.995}$-Sm$_{0.005}$GaB$_2$O$_7$ under different temperatures within 303–483 K (λ_{ex} = 370 nm). (b) Relationship of ln($I_0/I - 1$) versus $1/kT$ for this phosphor.

the slope of -0.211, so the activation energy ΔE is 0.211 eV. The relatively high activation energy obtained in this work indicates that this phosphor possesses good color thermal stability and can be recommended as a suitable candidate for high-power LED applications.

4. Conclusions

CdTbGaB$_2$O$_7$ is the first quaternary compound found in the CdO–Ln$_2$O$_3$–Ga$_2$O$_3$–B$_2$O$_3$ (Ln = rare-earth metals) system. It has a melilite-type structure, in which [B$_2$O$_7$]$^{8-}$ tetrahedral dimers and [GaO$_4$]$^{5-}$ tetrahedra share corners to generate 2D [Ga(B$_2$-O$_7$)]$_n^{5n-}$ layers that are further bridged by 8-coordinated (Cd^{2+}/Tb^{3+}) cations giving rise to a 3D framework. The IR and Raman studies supported the presence of B$_2$O$_7$ tetrahedral dimers and GaO$_4$ groups. The UV-vis absorption measurement of CdTbGaB$_2$O$_7$ showed the typical Tb^{3+} absorption peaks and the band gaps of 4.10 and 4.33 eV for indirect and direct transitions, respectively. Furthermore, a series of CdTb$_{1-x}$Sm$_x$GaB$_2$O$_7$ ($0 \leq x \leq 0.2$) phosphors was synthesized at 800 °C. Under the irradiation of 370 nm, the emission lines of Tb^{3+}: ^{5}D$_4 \rightarrow {}^7$F$_{6,5,4,3}$ and

Sm^{3+}: ^{4}G$_{5/2} \rightarrow {}^6$H$_{5/2,7/2,9/2,11/2}$ appeared simultaneously in the PL spectra of CdTb$_{1-x}$Sm$_x$GaB$_2$O$_7$. The emission intensity of Tb^{3+} at 545 nm decreased monotonously, while that of Sm^{3+} at 603 nm first increased and then declined with increasing Sm^{3+} content, showing the Tb$^{3+} \rightarrow$ Eu^{3+} energy transfer and the concentration quenching between Sm^{3+} ions. The optimized CdTb$_{0.995}$Sm$_{0.005}$GaB$_2$O$_7$ phosphor exhibited a QY of 13.22% and good thermal stability with ΔE of 0.211 eV. The luminescence color can be tuned from green to orange-red by changing the Sm^{3+} doping concentration, and these types of materials have potential as tunable luminescence materials to meet the application requirements for n-UV LEDs.

Conflicts of interest

There are no conflicts to declare.

Acknowledgements

References

1 L. P. Ogorodova, Y. D. Gritsenko, M. F. Vigasina, A. Y. Bychkov, D. A. Ksenofontov and L. V. Melchakova, *Am. Mineral.*, 2018, **103**, 1945–1952.

2 F. Rothlisberger, F. Seifert and M. Czank, *Eur. J. Mineral.*, 1990, **2**, 585–594.

3 C. Yin, Z. Yu, L. Shu, L. Liu, Y. Chen and C. Li, *J. Adv. Ceram.*, 2021, **10**, 108–119.

4 A. A. Kaminskii, H. R. Verdun and B. V. Mill, *Phys. Status Solidi A*, 1992, **129**, K125–K130.

5 M. Alam, K. H. Gooen, B. Di Bartolo, A. Linz, E. Sharp, L. Gillespie and G. Janney, *J. Appl. Phys.*, 1968, **39**, 4728–4730.

6 D. J. Horowitz, L. F. Gillespie, J. E. Miller and E. J. Sharp, *J. Appl. Phys.*, 1972, **43**, 3527–3530.

7 G. Giuli, L. Bindi and P. Bonazzi, *Am. Mineral.*, 2000, **85**, 1512–1515.

8 J. Barbier, N. Penin and L. M. Cranswick, *Chem. Mater.*, 2005, **17**, 3130–3136.

9 N. Li, P. Fu, Y. Wu and J. Zhang, *J. Cryst. Growth*, 2009, **311**, 3476–3478.

10 E. Erdoğmuş and E. Korkmaz, *Optik*, 2014, **125**, 4098–4101.

11 Q. Zhang, J. Wang, M. Zhang, W. Ding and Q. Su, *J. Rare Earths*, 2006, **24**, 392–395.

12 Q. Zhang, J. Wang, H. Ni and L. Wang, *Rare Met.*, 2012, **31**, 35–38.

13 D. Kasprowicz, K. Jaroszewski, P. Głuchowski, E. Michalski and A. Majchrowski, *J. Alloys Compd.*, 2021, **873**, 159772.

14 K. Jaroszewski, P. Gluchowski, M. G. Brik, T. Pedzinski, A. Majchrowski, M. Chrunik, E. Michalski and D. Kasprowicz, *Cryst. Growth Des.*, 2017, **17**, 3656–3664.

15 D. Kasprowicz, M. G. Brik, K. Jaroszewski, T. Pedzinski, B. Bursa, P. Głuchowski, A. Majchrowski and E. Michalski, *Opt. Mater.*, 2015, **47**, 428–434.

16 R. L. Tang, C. L. Hu, B. L. Wu, Y. Chen and J. G. Mao, *Inorg. Chem. Front.*, 2019, **6**, 2304–2310.

17 K. P. Mani, G. Vimal, P. R. Biju, C. Joseph, N. V. Unnikrishnan and M. A. Ittyachen, *Opt. Mater.*, 2015, **42**, 237–244.

18 K. Li and R. V. Deun, *Dalton Trans.*, 2018, **47**, 6995–7004.

19 W. Xie, G. Liu, X. Dong, J. Wang and W. Yu, *RSC Adv.*, 2015, **5**, 77866–77872.

20 W. Zhou, M. Gu, Y. Ou, C. Zhang, X. Zhang, L. Zhou and H. Liang, *Inorg. Chem.*, 2017, **56**(13), 7433–7442.

21 T. Skarzynski, M. Meyer and P. Stec, *Acta Crystallogr., Sect. A: Found. Crystallogr.*, 2011, **67**, C660–C661.

22 G. M. Sheldrick, *Acta Crystallogr., Sect. C: Struct. Chem.*, 2015, **71**, 3–8.

23 R. D. Shannon, *Acta Crystallogr., Sect. A: Cryst. Phys., Diffr., Theor. Gen. Crystallogr.*, 1976, **32**, 751–767.

24 A. L. Spek, *J. Appl. Crystallogr.*, 2003, **36**, 7–13.

25 T. Yamashita, T. Fujino, N. Masaki and H. Tagawa, *J. Solid State Chem.*, 1981, **37**, 133–139.

26 O. Muller and R. Roy, *Adv. Chem. Ser.*, 1971, **98**, 28–38.

27 R. R. Bian, X. A. Chen, W. Q. Xiao and X. Y. Song, *J. Lumin.*, 2022, **242**, 118545.

28 R. W. Smith, M. A. Kennard and M. J. Dudik, *Mater. Res. Bull.*, 1997, **32**, 649–656.

29 T. S. Ortner, D. Vitzthum, G. Heymann and H. Huppertz, *Z. Anorg. Allg. Chem.*, 2017, **643**, 2103–2109.

30 I. D. Brown and D. Altermatt, *Acta Crystallogr., Sect. B: Struct. Sci.*, 1985, **41**, 244–247.

31 J. Barbier and L. M. D. Cranswick, *J. Solid State Chem.*, 2006, **179**, 3958–3964.

32 X. A. Chen, Y. An and W. Q. Xiao, *J. Lumin.*, 2021, **237**, 118137.

33 N. Ye, W. R. Zeng, B. C. Wu, X. Y. Huang and C. T. Chen, *Z. Krist. - New Cryst. Struct.*, 1998, **213**, 452.

34 B. C. Cornilsen and R. A. Condrate sr, *J. Phys. Chem. Solids*, 1977, **38**, 1327–1332.

35 J. Hanuza, M. Maczka, M. Ptak, J. Lorenc, K. Hermanowicz, P. Becker, L. Bohaty and A. A. Kaminskii, *J. Raman Spectrosc.*, 2011, **42**, 782–789.

36 S. N. Achary, D. Errandonea, D. Santamaria-Perez, O. Gomis, S. J. Patwe, F. J. Manjón, P. R. Hernandez, A. Muñoz and A. K. Tyagi, *Inorg. Chem.*, 2015, **54**(13), 6594–6605.

37 S. Filatov, Y. Shepelev, R. Bubnova, N. Sennova, A. V. Egorysheva and Y. F. Kargin, *J. Solid State Chem.*, 2004, **177**, 515–522.

38 V. V. Atuchin, A. K. Subanakov, A. S. Aleksandrovsky, B. G. Bazarov, J. G. Bazarova, T. A. Gavrilova, A. S. Krylov, M. S. Molokeev, A. S. Oreshonkov and S. Y. Stefanovich, *Mater. Des.*, 2018, **140**, 488–494.

39 J. Li, S. P. Xia and S. Y. Gao, *Spectrochim. Acta, Part A*, 1995, **51**(4), 519–532.

40 H. Fan, G. Wang and L. Hu, *Solid State Sci.*, 2009, **11**, 2065–2070.

41 G. Whichard and D. E. Day, *J. Non-Cryst. Solids*, 1984, **66**, 477–487.

42 J. Ma, J. Chen, H. Xiang, J. Li, Y. Tang and L. Fang, *Ceram. Int.*, 2022, **48**, 6218–6224.

43 F. Baur, F. Glocker and T. Jüstel, *J. Mater. Chem. C*, 2015, **3**, 2054–2064.

44 X. Y. Chen, M. P. Jensen and G. K. Liu, *J. Phys. Chem. B*, 2005, **109**, 13991–13999.

45 Y. C. Li, Y. H. Chang, Y. F. Lin, Y. S. Chang and Y. J. Lin, *J. Alloys Compd.*, 2007, **439**, 367–375.

46 J. Tauc, R. Grigorovici and A. Vancu, *Phys. Status Solidi*, 1966, **15**, 627–637.

47 P. Y. Chen and G. Wang, *Solid State Sci.*, 2020, **108**, 106442.

48 P. Chen, M. M. Murshed and T. M. Gesing, *J. Mater. Sci.*, 2021, **56**, 3639–3652.

49 A. A. Coelho, *J. Appl. Crystallogr.*, 2018, **51**, 210–218.

50 Y. Purusothaman, N. R. Alluri, A. Chandrasekhar and S. J. Kim, *J. Mater. Chem. C*, 2017, **5**, 415–426.

51 N. X. Ca, N. D. Vinh, S. Bharti, P. M. Tan, N. T. Hien, V. X. Hoa, Y. Peng and P. V. Do, *J. Alloys Compd.*, 2021, **883**, 160764.

52 V. V. Atuchin, A. S. Aleksandrovsky, O. D. Chimitova, C. P. Diao, T. A. Gavrilova, V. G. Kesler, M. S. Molokeev, A. S. Krylov, B. G. Bazarov, J. G. Bazarova and Z. Lin, *Dalton Trans.*, 2015, **44**, 1805–1815.

53 R. T. Haasch, E. Breckenfeld and L. W. Martin, *Surf. Sci. Spectra*, 2014, **21**, 122–130.

54 V. V. Atuchin, S. V. Adichtchev, B. G. Bazarov, Zh. G. Bazarova, T. A. Gavrilova, V. G. Grossman, V. G. Kesler, G. S. Meng, Z. S. Lin and N. V. Surovtsev, *Mater. Res. Bull.*, 2013, **48**, 929–934.

55 S. Gu, W. Li, Y. Bian, F. Wang, H. Li and X. Liu, *J. Phys. Chem. C*, 2016, **120**, 19242–19251.

56 X. Zhang and H. J. Seo, *Mater. Res. Bull.*, 2012, **47**, 2012–2015.

57 D. Qin and W. Tang, *RSC Adv.*, 2017, **7**, 2494–2502.

58 Q. Cheng, Y. Dong, M. Kang and P. Zhang, *J. Lumin.*, 2014, **156**, 91–96.

59 X. A. Chen, R. R. Bian, W. Q. Xiao and X. Y. Song, *Dalton Trans.*, 2022, **51**, 9454–9466.

60 X. Liu, S. Chen and X. Wang, *J. Lumin.*, 2007, **127**, 650–654.

61 J. Chen, J. Wang, F. Zhang, D. Yan, G. Zhang, R. Zhuo and P. Yan, *J. Phys. D: Appl. Phys.*, 2008, **41**, 105306.

62 Z. Li, B. Zhong, Y. Cao, S. Zhang, Y. Lv, Z. Mu, Z. Hu and Y. Hu, *J. Mater. Sci.: Mater. Electron.*, 2019, **30**, 10491–10498.

63 Z. Zhu, G. Fu, Y. Yang, Z. Yang and P. Li, *J. Mater. Sci.*, 2016, **51**, 6944–6954.

64 Q. Ren, Y. Zhao, X. Wu and O. Hai, *Polyhedron*, 2020, **192**, 114862.

65 R. Shrivastava, J. Kaur and V. Dubey, *J. Fluoresc.*, 2016, **26**, 105–111.

66 C. S. McCamy, *Color Res. Appl.*, 1992, **17**, 142–144.

67 G. Annadurai, B. Devakumar, H. Guo, B. Li, L. Sun and X. Huang, *RSC Adv.*, 2018, **8**, 30396–30403.

68 X. Min, Z. Huang, M. Fang, Y. G. Liu, C. Tang and X. Wu, *Inorg. Chem.*, 2014, **53**, 6060–6065.

69 F. Jensen, *Qual. Reliab. Eng. Int.*, 1985, **1**, 13–17.